

Strain-Induced Distortions Modulate the Optoelectronic Properties of Epitaxial BiVO₄ Films

Erwin N. Fernandez, Daniel A. Grave, Roel van de Krol, and Fatwa F. Abdi*

Transition metal oxide (TMO) photoabsorbers are expected to play an important role in the development of renewable solar-to-fuel devices. Modest efficiencies have been demonstrated with devices based on TMO photoabsorbers, and further progress will likely rely on material property control beyond conventional bulk chemistry or nanostructuring strategies. To this end, model TMO photoabsorbers such as single crystalline monoclinic bismuth vanadate (BiVO₄) are beneficial to advance the understanding of structure-functionality relationships with minimal convoluted effects inherent in polycrystalline systems. Here, the authors reveal for the first time the effects of strain modulation strategies on the optoelectronic properties of epitaxial BiVO₄ films synthesized by alternate-target layer-by-layer pulsed laser deposition. Through a combination of high-resolution X-ray diffraction methods and optical and photoluminescence spectroscopies, the correlation between anisotropic, uniaxial strain-driven bandgap widening and deviatoric strains associated with volume-preserving lattice distortions is established. Broad polaronic photoluminescence signals are detected in epitaxial BiVO₄, and its redshift is attributed to the structural distortion in BiO₈ dodecahedra. Overall, the relationship between the structural and optoelectronic properties revealed in this study suggests that strain modulation and engineering of local distortion in complex transition metal oxides may be exploited as a viable strategy for the development of efficient photoabsorbers.

1. Introduction

Transition metal oxides (TMOs) are interesting candidates as photoabsorbers in solar energy-to-fuels conversion and photocatalysis applications, based on their wide compositional space for bandgap tunability, relative stability in aqueous environments, and low cost. These oxides have successfully been implemented in a number of demonstration devices, for example, as a top wide-bandgap ($E_g > 1.8$ eV) photoabsorber in solar fuel generators with tandem configuration.^[1] Monoclinic bismuth vanadate (BiVO₄) in particular has emerged as a promising TMO photoanode in recent decades and is considered an excellent material platform for which targeted strategies for material property control in TMOs could be studied and implemented, both at the material discovery^[2] and device scale-up levels.^[3,4] Various bulk chemical modifications (e.g., doping) and nanostructuring strategies have been implemented in state-of-the-art BiVO₄ photoanodes to enhance its optoelectronic and photoelectrochemical properties, thus driving its

water oxidation photocurrents to near-theoretical maximum levels (7.5 mA·cm⁻², assuming all AM1.5 photons with energy larger than the bandgap $E_g \approx 2.4$ –2.5 eV of BiVO₄ are collected).^[5–8]

Despite the progress mentioned above, one particular aspect that is still poorly understood, especially in the case of BiVO₄, is the impact of epitaxial strain modulation on its optoelectronic properties. When exploited, this strategy has the potential to tailor and optimize the photoabsorber's interaction with light. Indeed, epitaxial strain-modulation of optoelectronic properties has been well-demonstrated in classical group IV photoabsorbers such as Si and Ge,^[9,10] III-V photoabsorbers such as GaAs,^[11] and perovskite oxides^[12,13] and halides,^[14] along with concomitant changes to its carrier transport properties.^[15–17] Here, we report for the first time the effects of epitaxial strain modulation on the optoelectronic properties of BiVO₄ probed using the combination of high-resolution X-ray characterization methods coupled with optical and photoluminescence spectroscopies. Using alternate-target layer-by-layer pulsed laser deposition (PLD), which offers better control of stoichiometry compared to conventional PLD,^[18–21] single-crystalline epitaxial BiVO₄ films deposited on yttrium stabilized zirconia (YSZ) are used as a

E. N. Fernandez, R. van de Krol, F. F. Abdi
Institute for Solar Fuels
Helmholtz-Zentrum Berlin für Materialien und Energie GmbH
Hahn-Meitner-Platz 1, 14109 Berlin, Germany
E-mail: fatwa.abdi@helmholtz-berlin.de

E. N. Fernandez, R. van de Krol
Institute of Chemistry
Technische Universität Berlin
Straße des 17. Juni 124, 10623 Berlin, Germany

D. A. Grave
Department of Materials Engineering and Ilse Katz Institute for Nanoscale Science and Technology
Ben Gurion University of the Negev
Be'er Sheva 8410501, Israel

 The ORCID identification number(s) for the author(s) of this article can be found under <https://doi.org/10.1002/aenm.202301075>

© 2023 The Authors. Advanced Energy Materials published by Wiley-VCH GmbH. This is an open access article under the terms of the Creative Commons Attribution License, which permits use, distribution and reproduction in any medium, provided the original work is properly cited.

DOI: 10.1002/aenm.202301075

well-defined model system to isolate the intrinsic effects of strain from extrinsic complications arising from the presence of grain boundaries or secondary phases inherent in polycrystalline materials. Systematically modulating the strain through thickness-dependent studies reveals how the anisotropic, uniaxial strain imposed by the substrate drives the evolution of structural and optoelectronic properties of epitaxial BiVO₄ films. We demonstrate through strain tensor decomposition analysis that the bandgap widening with increasing in-plane compressive strain is correlated to deviatoric strains associated with volume-preserving lattice distortions. We finally establish the correlation between the redshift in the broad, polaronic photoluminescence emission with structural BiO₈ unit distortions, which is crucial in the complete understanding of the optoelectronic properties in BiVO₄. Our results reveal the key role of structural distortions via epitaxial strain modulation strategies in controlling the optoelectronic properties in TMOs.

2. Experimental Section

Epitaxial BiVO₄ thin films were synthesized using alternate-target layer-by-layer pulsed laser deposition^[18] to enable better control of the stoichiometry to within 1–2% and reduce the overall complexity associated with conventional PLD.^[19–21] Film thicknesses of 8.8, 13.6, 23.7, 52.7, and 76.9 nm were deposited using a custom-built PLD setup (PREVAC, Rogów, Poland) with the growth chamber pumped down to a base pressure of $\approx 10^{-7}$ mbar. A KrF excimer laser ($\lambda = 248$ nm, pulse duration 20 ns, Coherent LPXpro 210, Santa Barbara, CA, USA) was used to ablate 4N-pure Bi₂O₃ and V₂O₅ sintered targets (FHR, Ottendorf-Okrilla, Germany). Films were deposited on double-sided polished (001)-oriented YSZ substrates (8% mol Y₂O₃, Alineason, Frankfurt, Germany). The deposition was done in an off-axis configuration to ensure thickness uniformity; this was confirmed by the negligible variation in the UV–vis transmission spectra taken at different locations on the sample (see Figure S1, Supporting Information – estimated thickness standard deviation ± 0.2 nm for the 8.8 nm film to ± 0.9 nm for the 76.9 nm film). A substrate temperature of 700 °C resulted in the highest quality film, as quantified by the width of the BiVO₄ (004) reflection in a rocking curve scan. An oxygen background pressure of $p(\text{O}_2) = 25$ mtorr (0.033 mbar) was imposed to modulate the propagation and kinetic energy distribution of the plasma plume. At the given substrate temperature and $p(\text{O}_2)$, the substrate-to-target distance was set to the plasma plume range^[22] $L_0 = 5.6$ cm such that the plume was thermalized upon reaching the substrate surface. A laser repetition rate of 1 Hz was used during ablation. To build a monolayer thick (11.7 Å) BiVO₄ film, a cycle consisting of 42 pulses of V₂O₅ at a laser fluence of 2 J·cm⁻² and 16 pulses of Bi₂O₃ at a laser fluence of 0.75 J·cm⁻² was required, with a 30 s annealing step at the end of the cycle. The number of pulses required was determined by a procedure similar to the one outlined in Lei et al.^[23] The cycle was repeated a number of times to build films of desired thicknesses. After deposition, the films were cooled down to room temperature at a rate of 12 °C·min⁻¹ while maintaining the same $p(\text{O}_2)$ of 25 mtorr. No post-deposition annealing was performed on the films.

To establish the phase and crystalline quality of the films, their epitaxial relationship, and lattice parameters (a , b , c , γ),

high-resolution X-ray diffraction (HR-XRD) was performed on a Philips PANalytical X'Pert Pro MRD in four-circle, triple-axis configuration. A four-bounce Ge(220) Bartels monochromator conditioned the incident X-ray beam from a Cu X-ray tube to yield Cu $K\alpha_1$ radiation ($\lambda = 1.5406$ Å). Bragg reflections were aligned to the YSZ(002) diffraction peak as a reference and were detected by a PreFIX line detector. X-ray reflectivity (XRR) measurements were taken using Cu $K\alpha$ radiation ($\lambda = 1.5418$ Å) in parallel beam geometry, after which the XRR data was analyzed using GenX^[24] to extract the film thickness and roughness.

To determine the optical constants of the BiVO₄ films, UV–vis transmittance and near normal-incidence (8°) reflectance spectroscopy were performed on a Perkin–Elmer Lambda 950 spectrophotometer, equipped with an integrating sphere and a photomultiplier tube detector. The spectrophotometer was wavelength-calibrated against the D₂ emission line ($\lambda = 656.1$ nm). Prior to measurements, adjustments to 0% and 100% transmission levels without any sample in the beampath were determined. Reflectance measurements were referenced against a Spectralon reference standard (Labsphere SRS-99-020, New Hampshire, USA). Due to the multiple interference effects between interfaces, simplified expressions for the calculation of absorption coefficient α (Lambert–Beer) yielded inconsistent results among samples; hence, the calculation of α required extracting the optical constants (refractive index n and extinction coefficient k) using the more rigorous transfer matrix method as implemented in RefDEX.^[25] As the extraction procedure was an ill-posed problem that might yield numerous unphysical solutions, both film-incident (R) and substrate-incident (R') reflectance spectra were acquired on top of the transmittance (T) spectra to guarantee self-consistent convergence to the correct n and k values during the transfer matrix method calculations. The extracted optical constants were verified to be Kramers–Kronig consistent via constrained variational Kramers–Kronig analysis using Drude–Lorentz oscillators as implemented in RefFIT^[26] (see Figure S2, Supporting Information). The absorption coefficient was then calculated from the extinction coefficient as $\alpha = 4\pi k/\lambda$.

Photoluminescence (PL) emission spectra of the epitaxial BiVO₄ films were collected at room temperature. Samples were excited with a pulsed diode laser (PicoQuant, Berlin, Germany) at 405 nm with a laser spot radius of ≈ 10 μm , and a typical laser power density of 200 mW·cm⁻². The PL emission was dispersed by a 0.5 m grating monochromator and detected with a Peltier-cooled CCD detector (Newton EMCCD, Andor, Belfast, UK).

3. Results and Discussion

An essential consideration to achieve highly-oriented epitaxial growth of BiVO₄ is the proper choice of substrate that is lattice-matched to the in-plane lattice parameters of BiVO₄. For this purpose, cubic YSZ with 8 mol% Y₂O₃ ($Fm\bar{3}m$, lattice parameter $a = 5.1424$ Å^[27]) provides an excellent lattice match to monoclinic BiVO₄ ($I2/b$, $a = 5.1956$ Å, $b = 5.0935$ Å, $c = 11.7$ Å, and $\gamma = 90.383^\circ$ ^[28]). The lattice mismatch $(a_{\text{YSZ}} - a_{\text{film}})/a_{\text{film}}$, in this case, is -1.0% along [100]_{YSZ} and 1.0% along [010]_{YSZ}. BiVO₄ growth in the [001] direction is thus anticipated on YSZ(001). On top of this, since YSZ(001) grows epitaxially on Si(100),^[29–32] ITO,^[33,34] and mica,^[35,36] the choice of YSZ(001) as the substrate makes it relevant as a possible epitaxial buffer layer in realizing a

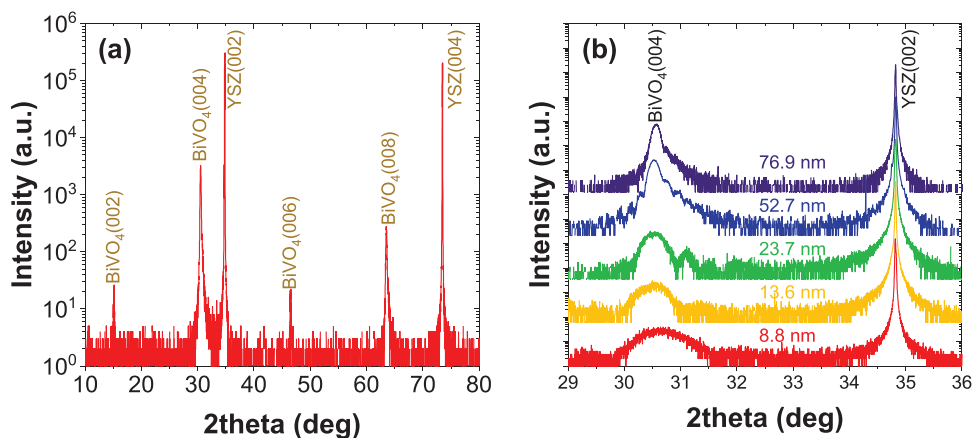


Figure 1. a) Typical out-of-plane $2\theta/\omega$ diffraction pattern of BiVO_4 epitaxial thin films deposited on YSZ substrates showing (00 l) reflections, indicating out-of-plane growth in the [001] direction. b) High-resolution $2\theta/\omega$ scan of the BiVO_4 (004) reflection of films with varying thickness. The interference fringes around the BiVO_4 (004) peak indicate atomically smooth films.

number of possible all-epitaxial photoelectrochemical (PEC) device configurations, ranging from monolithic $m\text{-BiVO}_4/\text{YSZ}/n\text{-Si}$ integrated PEC tandem devices,^[37] to flexible PEC devices on mica. **Figure 1a** shows the typical X-ray diffraction pattern of the BiVO_4 films deposited on YSZ(001). Only reflections indexed to BiVO_4 (00 l) planes are found, indicating that BiVO_4 film grew epitaxially in the [001] direction. The (002) peak at $2\theta = 15.16^\circ$ indicates the successful growth of the monoclinic polymorph, as this peak is forbidden in the tetragonal polymorph.^[38] Also, the presence of the $\approx 828\text{ cm}^{-1}$ peak in the Raman spectra further confirms the monoclinic polymorph (see Note S1 and Figure S3, Supporting Information).^[39]

We further investigated the effect of increasing film thickness on the crystal structure of the epitaxial BiVO_4 films by performing high-resolution XRD measurements **Figure 1b**). A slight increase in the 2θ position of the BiVO_4 (004) peak is observed, which indicates weak contraction of the out-of-plane lattice pa-

rameter with increasing film thickness. All films are phase-pure: no extraneous peaks attributable to unreacted Bi_2O_3 or V_2O_5 , nor any parasitic phases are present. Moreover, the presence of Pendellösung fringes around the symmetric BiVO_4 (004) peak shown in the high-resolution XRD scan in **Figure 1b** indicates atomically smooth films, with a roughness of $< 2.5\text{ nm}$ as determined from XRR (**Figure S4**, Supporting Information) and atomic force microscopy (AFM, **Figure S5**, Supporting Information).

The excellent crystalline quality of the epitaxial BiVO_4 films is further established in the rocking curves for the BiVO_4 (004) symmetric peak shown in **Figure 2a**. In the limit of crystalline perfection, single crystals would exhibit a sharp rocking curve that is only limited by instrumental broadening. On the other hand, the presence of defects and structural imperfections that lower the crystalline quality (e.g., dislocations) broadens the rocking curve. Both these sharp and broad peaks (termed coherent and diffuse components, respectively) may be present in the

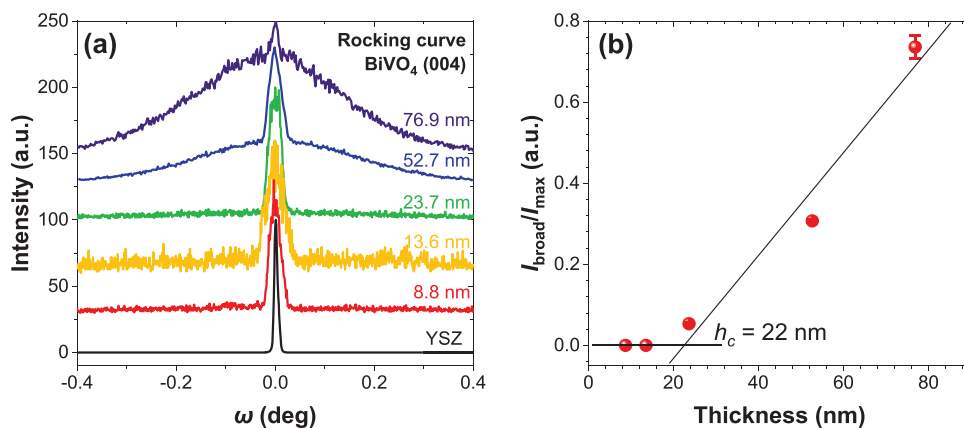


Figure 2. a) Rocking curves (ω -scan) of the symmetric BiVO_4 (004) peak for BiVO_4 films with varying thicknesses on YSZ substrates. The rocking curve of the symmetric YSZ(002) peak for the YSZ substrates is also shown. Thinner BiVO_4 films exhibit sharp rocking curves with FWHM values close to that of the substrate. A broad Gaussian background peak (FWHM $\approx 0.35\text{--}0.37^\circ$) emerges with increasing film thickness, suggesting a relaxation of the film. Note that the rocking curves are normalized and shifted for clarity. b) Plot of the intensity of the broad peak relative to the rocking curve peak maximum ($I_{\text{broad}}/I_{\text{max}}$) versus film thickness. The estimated critical thickness at which film relaxation occurs is $h_c = 22\text{ nm}$. Error bars correspond to standard errors.

rocking curve in superposition to each other, which reflects the density of dislocations in the relaxed regions of the film.^[40] For all the BiVO₄ film thicknesses studied, the rocking curves shown in Figure 2a exhibit a sharp central peak (full width at half maximum, FWHM ≈ 0.016 – 0.042°) that closely resembles the peak of the YSZ(002) rocking curve of the substrate (FWHM $\approx 0.010^\circ$). We note that the high crystalline quality of the BiVO₄ films obtained in this study rivals that of MBE-grown epitaxial BiVO₄ films as reported by Stoughton et al.,^[38] demonstrating the capabilities of alternating-target PLD as a technique to produce high-quality, single-crystalline films.

Superimposed against the sharp central peaks in the rocking curves in Figure 2a is a broad Gaussian background of nearly constant FWHM (≈ 0.35 – 0.37°) that is notably absent in the thinner films and emerges at a particular film thickness. The critical thickness (h_c) is estimated to be 22 nm, obtained by plotting the intensity of the broad peak relative to the rocking curve peak maximum ($I_{\text{broad}}/I_{\text{max}}$) as a function of the film thickness (Figure 2b). Similar features were observed in epitaxial EuO(001)/YAlO₃(110) films.^[41] In the ultrathin regime, epitaxial films can grow pseudomorphically as the film accommodates elastic energy and deforms to match the in-plane lattice parameters of the substrate. As the film grows beyond the critical thickness, however, the stored elastic energy in the film would be greater than the energy required to create misfit dislocations. As a result, the film would undergo plastic relaxation with concomitant formation of misfit dislocations and defects during the process.^[42] The appearance of the broad background, that is, the diffuse component, in the BiVO₄(004) rocking curves in Figure 2a for films thicker than $h_c = 22$ nm reflects this very process – the film undergoing relaxation, forming defects that lower the crystalline quality.

The ensuing relaxation in BiVO₄ epitaxial films is intimately tied to the evolution of the in-plane strain that the film experiences. From the lattice mismatch values between that of BiVO₄ and YSZ (vide supra), one can infer that the BiVO₄ film would experience anisotropic in-plane strain: compressive strain in the [100] direction and tensile strain in the [010] direction. However, the exact deformation state of the film may not be discerned from lattice mismatch values alone. In order to reveal more details on the anisotropic in-plane strain relaxation and the strain scenario that occurs in our films with increasing thickness, reciprocal space maps (RSMs) of the asymmetric BiVO₄(208) and (028) reflections relative to the YSZ(204) reflection were obtained, as shown in Figure 3. This method has been indicated as the gold standard in demonstrating the epitaxial relationship between the deposited films and the substrates.^[43] First, the RSMs of the BiVO₄(208) and (028) reflections establish the in-plane relationship of the BiVO₄ films to the YSZ substrate: BiVO₄[100] || YSZ[100], BiVO₄[010] || YSZ[010]. Moreover, the RSMs also clearly depict whether the film is strained to the substrate or relaxed as a function of film thickness. For the 8.8 nm film, the RSM exhibits a single sharp BiVO₄ peak, with coincident in-plane components for the BiVO₄(208) and YSZ(204) reflections ($Q_{x[100]} \approx 2.441 \text{ \AA}^{-1}$), indicating that the film is clamped in the [100] direction. The in-plane component of the BiVO₄(028) reflection, however, is at BiVO₄ bulk values ($Q_{x[010]} \approx 2.469 \text{ \AA}^{-1}$), indicating that the film is relaxed in the [010] direction. RSMs of films 13.6 nm and thicker still exhibit a central peak but with increased broadening on the shoulders, consistent with film relaxation via mis-

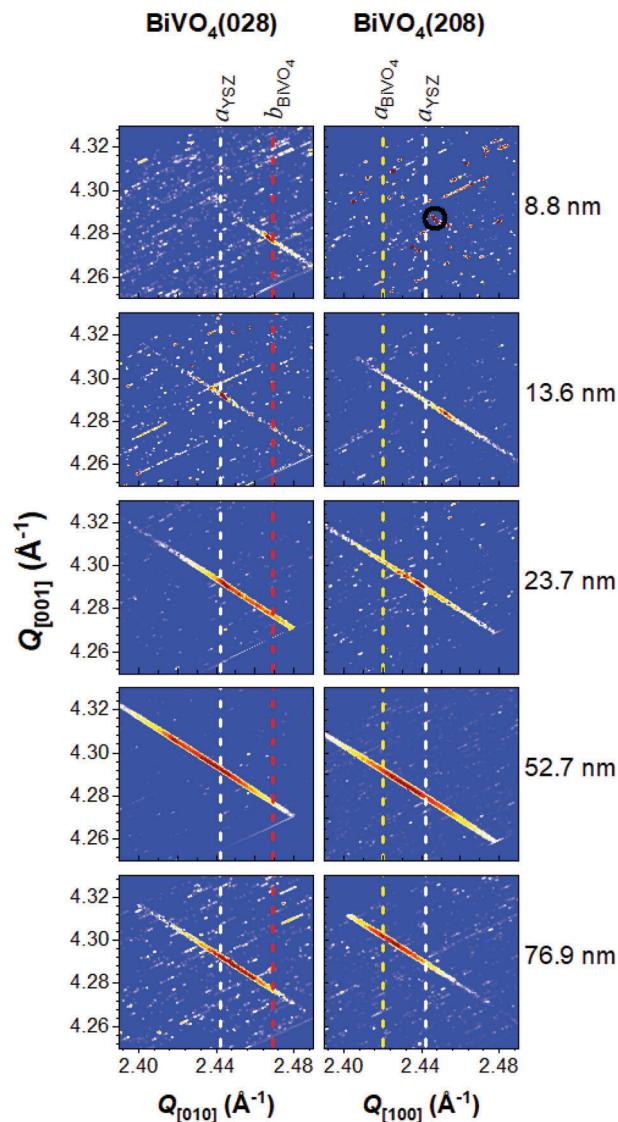


Figure 3. Reciprocal space maps of the (028) and (208) reflections of the BiVO₄ films of varying thicknesses on YSZ substrates. Due to its relatively weak intensity, the peak of the (208) reflection for the 8.8 nm film (top-most right plot) is marked with a circle to aid visualization. The white vertical dashed lines depict the in-plane component of the YSZ(204) reflection (a_{YSZ} at $Q_x = 2.441 \text{ \AA}^{-1}$). The orange-red and yellow vertical dashed lines depict the bulk values of the in-plane components of BiVO₄(028) and (208) (b_{BiVO_4} at $Q_{[010]} = 2.469 \text{ \AA}^{-1}$ and a_{BiVO_4} at $Q_{[100]} = 2.42 \text{ \AA}^{-1}$), respectively.

fit dislocations. For these films, the in-plane component of the BiVO₄(028) reflection is equal to the YSZ(204) reflection ($Q_{x[010]} \approx 2.441 \text{ \AA}^{-1}$), indicating that the film is now clamped in the [010] direction; however, the in-plane component of the BiVO₄(208) reflection shifts towards BiVO₄ bulk values ($Q_{x[100]} \approx 2.420 \text{ \AA}^{-1}$), indicating relaxation of the film in the [100] direction.

The thickness dependence of the lattice parameters (a , b , c , γ) of the BiVO₄ films—extracted from the RSMs—is summarized in Figure 4a–c. The film lattice parameter a monotonically relaxes towards the BiVO₄ bulk value ($a_{\text{bulk, BiVO}_4} = 5.196 \text{ \AA}$), albeit partially. The degree of film relaxation $R_m = \frac{a - a_{\text{bulk, YSZ}}}{a_{\text{bulk, BiVO}_4} - a_{\text{bulk, YSZ}}}$ only

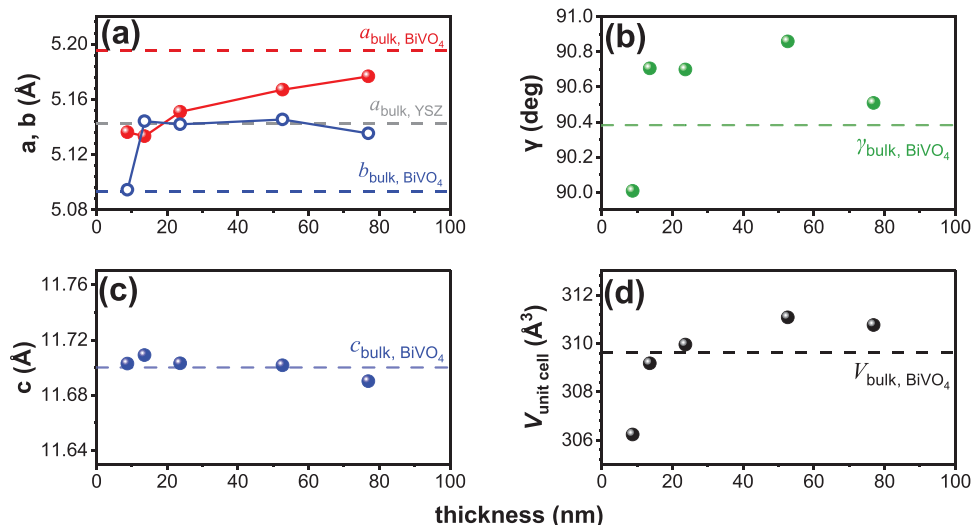


Figure 4. a) In-plane lattice parameters (*a*, *b*), b) out-of-plane lattice parameter (*c*), c) monoclinic angle γ , and d) calculated unit cell volume V_{uc} as a function of the BiVO₄ film thickness. YSZ lattice parameters, bulk BiVO₄ lattice parameters, and bulk BiVO₄ unit cell volume are depicted by dashed lines for comparison. Errors in lattice parameters and unit cell volumes are $< 0.005 \text{ \AA}$ and $< 0.7 \text{ \AA}^3$, respectively; these values are not visible in the plots since they are smaller than the size of the data markers.

reaches 0.64 for the thickest (76.9 nm) film. The film lattice parameter *b*, on the other hand, exhibits minimal relaxation with film thickness and is virtually fixed to the lattice parameter of the substrate ($b \approx a_{\text{bulk, YSZ}} = 5.1424 \text{ \AA}$). The film out-of-plane lattice parameter *c* slightly decreases with film thickness and remains close to the BiVO₄ bulk value ($c_{\text{bulk, BiVO}_4} = 11.7 \text{ \AA}$). The corresponding unit cell volumes ($V_{uc} = abc \sin \gamma$) of the films are presented in Figure 4d. The film thickness dependence of the linear strains ϵ_{xx} , ϵ_{yy} , ϵ_{zz} , and the shear strain ϵ_{xy} could therefore be calculated from the lattice parameters *a*, *b*, *c*, and γ .

$$\epsilon_{xx} = (a - a_{\text{bulk, BiVO}_4}) / a_{\text{bulk, BiVO}_4} \quad (1)$$

$$\epsilon_{yy} = (b - b_{\text{bulk, BiVO}_4}) / b_{\text{bulk, BiVO}_4} \quad (2)$$

$$\epsilon_{zz} = (c - c_{\text{bulk, BiVO}_4}) / c_{\text{bulk, BiVO}_4} \quad (3)$$

$$\epsilon_{xy} = \tan \left(\frac{\gamma_{\text{bulk, BiVO}_4} - \gamma}{2} \right) \quad (4)$$

Figure 5 shows that only ϵ_{xx} shows a strong thickness dependence. This suggests that the substrate-imposed anisotropic in-plane strain effectively results in strain relaxation that is uniaxial in nature with strain relief primarily along the [100] direction.

We note that additional information regarding the effect of the anisotropic in-plane strain on the lattice deformation can be observed from the V_{uc} trend in Figure 4d. Pseudomorphic growth of the thin 8.8 nm film led to the reduction in unit cell volume. With increasing film thickness, the unit cell volume rapidly reaches the BiVO₄ bulk value (309.6 Å³), within limits of experimental error. The rapid increase of V_{uc} between the film thicknesses of

8.8 and 13.6 nm closely parallels the jump in *b* and γ with thickness: *b* jumps from the BiVO₄ bulk value (5.096 Å) to the YSZ *a* lattice parameter (5.142 Å), while γ jumps from 90° to 90.7°, before gradually decreasing to the BiVO₄ bulk value (90.4°) with increasing film thickness.

4. Optical Properties

We then investigated the impact of anisotropic in-plane strain on the optical properties of BiVO₄ epitaxial thin films, and ultimately, on the electronic structure of BiVO₄. Preliminary UV-vis characterizations (data not shown) of the films studied here showed negligible contributions from diffuse transmittance and diffuse reflectance, and predominantly from specular contributions. This is a further indication of the film's low roughness and high surface quality, which is consistent with the XRR and AFM results.

Figure 6a shows the optical constants (refractive index *n* and extinction coefficient *k*) of the BiVO₄ films with varying thickness, extracted from the transmittance (*T*) and reflectance (*R*) spectra (Figure S6, Supporting Information). The calculated absorption coefficients α are presented in Figure 6b. A striking feature can be observed. For films with thickness $> h_C$, the optical constant and absorption coefficient curves practically overlap with each other. Below h_C the values of *n* and *k*, and the absorption coefficient α decrease over the whole wavelength range. At $\approx 430 \text{ nm}$, for instance, where the peak of the refractive index curves and the inflection point of the extinction coefficient are approximately located, *n* decreases by $\approx 10\text{--}25\%$ from that of thicker films, and the reduction for *k* and α is even more pronounced ($\approx 50\%$). Such thickness-dependent spectral variation of the optical constants for BiVO₄ shown here is not trivial and is important in the accurate design and modeling of solar fuel device characteristics.

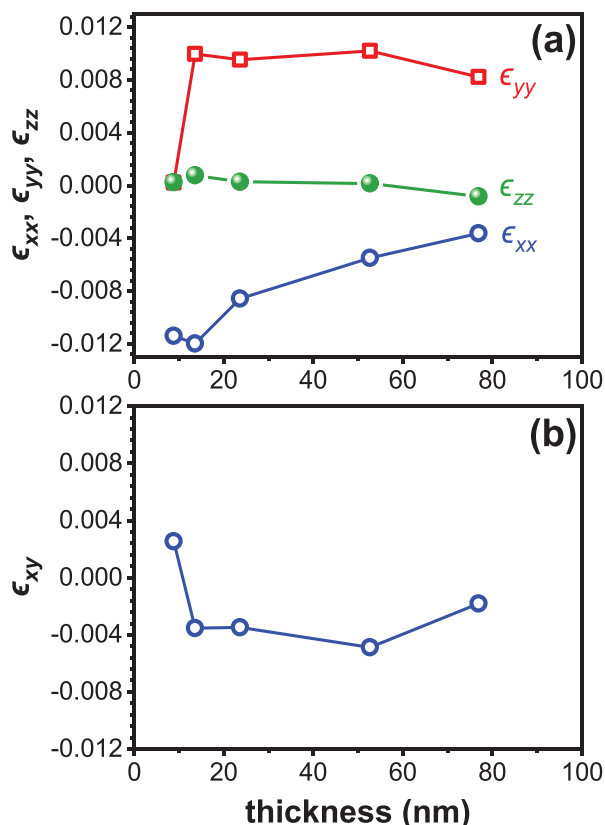


Figure 5. Variation in a) linear strains (ϵ_{xx} , ϵ_{yy} , ϵ_{zz}) and b) shear strain (ϵ_{xy}) as a function of film thickness.

In order to estimate the optical bandgap of the BiVO_4 epitaxial films, the direct and indirect bandgaps are then determined from Tauc analysis. **Figure 7a** shows the derived indirect and direct bandgaps plotted against the respective compressive in-plane strain along [100], ϵ_{xx} . Linear correlations with a slope of -38.5 meV per % strain and -20.8 meV per % strain can be observed for the direct and indirect bandgaps, respectively. This linear dependence, that is, increasing the compressive in-plane strain along [100] direction widens the bandgap of epitaxial BiVO_4 films, suggests that the bandgap shifts observed here are strain-driven,^[44] and not arising from quantum confinement effects (see Note S3, Supporting Information).

Exploring any possible correlation of the strain components to the bandgaps would be insightful at this point. To this end, we decompose the strain tensor ϵ_{ij} for monoclinic BiVO_4 ^[45] into its hydrostatic ϵ_H , and deviatoric components ϵ^* and ϵ' .

$$\epsilon_{ij} = \begin{bmatrix} \epsilon_{xx} & \epsilon_{xy} & 0 \\ \epsilon_{xy} & \epsilon_{yy} & 0 \\ 0 & 0 & \epsilon_{zz} \end{bmatrix} = \begin{bmatrix} \bar{\epsilon} & 0 & 0 \\ 0 & \bar{\epsilon} & 0 \\ 0 & 0 & \bar{\epsilon} \end{bmatrix} + \begin{bmatrix} \epsilon_{xx} - \bar{\epsilon} & 0 & 0 \\ 0 & \epsilon_{yy} - \bar{\epsilon} & 0 \\ 0 & 0 & \epsilon_{zz} - \bar{\epsilon} \end{bmatrix} + \begin{bmatrix} 0 & \epsilon_{xy} & 0 \\ \epsilon_{xy} & 0 & 0 \\ 0 & 0 & 0 \end{bmatrix} = \epsilon_H + \epsilon^* + \epsilon' \quad (5)$$

Here, the magnitude of the hydrostatic strain ϵ_H is related to the bulk volume changes of the lattice, as follows.

$$\bar{\epsilon} = \frac{1}{3} (\epsilon_{xx} + \epsilon_{yy} + \epsilon_{zz}) = \frac{1}{3} \frac{\Delta V}{V} \quad (6)$$

The deviatoric strain component ϵ^* is related to the changes in lengths in lattice parameters, while ϵ' is related to the changes in the monoclinic angle γ .

$$r(\epsilon^*)^2 = \frac{1}{3} \left[(\epsilon_{xx} - \epsilon_{yy})^2 + (\epsilon_{xx} - \epsilon_{zz})^2 + (\epsilon_{yy} - \epsilon_{zz})^2 \right] \quad (7)$$

$$(\epsilon')^2 = 2(\epsilon_{xy})^2 \quad (8)$$

We first compare the observed bandgap trends to lattice volume changes associated with an equivalent hydrostatic deformation. Semiconductor bandgaps respond to hydrostatic lattice deformations, as described by the material's bandgap deformation potential^[44] $\alpha_V = \frac{\partial E_g}{\partial \ln V}$: a change in the unit cell volume $\Delta V/V$ leads to a change in the bandgap $\Delta E_g = \alpha_V \frac{\Delta V}{V}$. Negative values of α_V exhibited by a number of classical semiconductors^[46] would imply a widening of the bandgap for a bulk contraction of the unit cell volume. Positive values of α_V , on the other hand, would imply the opposite – a narrowing of the bandgap for a bulk contraction of the unit cell volume. Such behavior is experimentally shown for related scheelite orthovanadates MVO_4 ,^[47] and theoretically predicted from high-pressure first-principles calculations for SnWO_4 .^[48] In our case, however, both the direct and indirect bandgaps weakly correlate with the hydrostatic strain ϵ_H (see **Figure 7b**, $r^2 = 0.027$ and 0.0007 , respectively), suggesting that hydrostatic strain effects are not sufficient to explain the dependence of bandgaps with thickness.

We then consider the correlation of the observed bandgaps with the deviatoric components of the strain tensor $(\epsilon^*)^2$ and $(\epsilon')^2$, the plots of which are depicted in **Figure 7c,d**, respectively. While the hydrostatic component describes the volume-changing (dilatory) effects associated with the strain, the deviatoric components, on the other hand, describe the volume-preserving and shape-distorting effects associated with the strain.^[49] The direct and indirect bandgaps of our epitaxial BiVO_4 correlate strongly with $(\epsilon^*)^2$ ($r^2 = 0.92$ and 0.82 , respectively), but weakly with $(\epsilon')^2$ ($r^2 = 0.02$ and 0.12 , respectively). The weak correlation of the bandgaps with $(\epsilon')^2$ seems to be supported by the electronic structure calculations of Newhouse et al.^[50] for stoichiometric $m\text{-BiVO}_4$ as a function of the monoclinic angle γ , which suggests that the bandgap is weakly sensitive to changes in the monoclinic angle. The larger the magnitude of the deviatoric strain $(\epsilon^*)^2$, the wider the bandgap becomes. This hints at the role of volume-preserving lattice distortions on the optical properties of BiVO_4 , possibly related to the distortion of the structural polyhedra that make up the BiVO_4 lattice, that is, BiO_8 dodecahedra and VO_4 tetrahedra.

Photoluminescence spectroscopy further probes into the effect of anisotropic in-plane strain on the electronic structure of BiVO_4 . The PL emission spectra of the epitaxial BiVO_4 thin films upon 405 nm excitation, shown in **Figure 8a** (see **Figure S7** and **Note S4**, Supporting Information for the raw spectra and the data extraction method), exhibit a spectrally narrow doublet B_1 and B_2 centered around 470 nm (2.63 eV) and 484 nm (2.56 eV), respec-

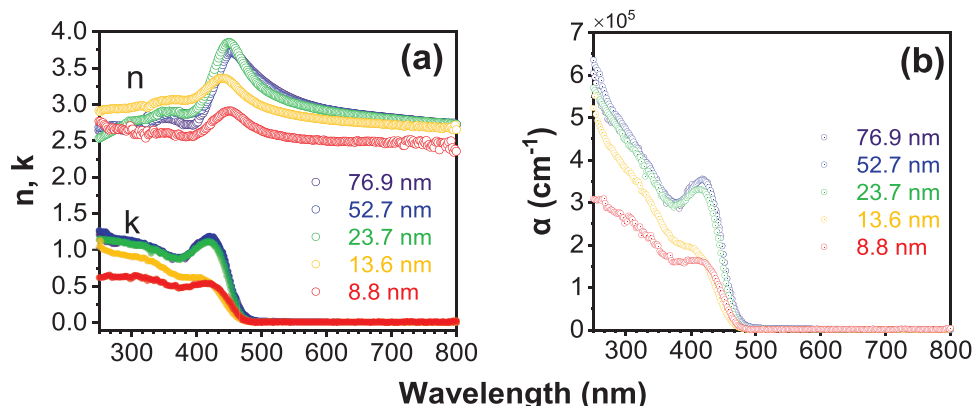


Figure 6. a) Optical constants – refractive index n and extinction coefficient k – of epitaxial BiVO_4 thin films as a function of thickness. b) Calculated absorption coefficient α as a function of film thickness.

tively, and a broad, asymmetric emission band which can be deconvoluted into two Gaussian peaks: A_1 centered around 635 nm (1.95 eV, FWHM 113–143 nm), and A_2 centered around 705 nm (1.75 eV, FWHM 62–77 nm). This broad emission band has also been reported in a number of studies on BiVO_4 powders^[51,52] and on electrodeposited polycrystalline BiVO_4 thin films on FTO glass.^[53] The intensity of the emission peaks weakens linearly with decreasing thickness, with the B_2 emission peak practically absent in the 8.8 and 13.6 nm films. Figure 8b shows the shifts in the A_1 and A_2 emission band positions with thickness. While the B_1 and B_2 peak positions are relatively unchanged with film thickness (as expected given the 20 meV bandgap shift in Figure 7a corresponds to only an ≈ 4 nm shift in the PL peak position), the A_1 and A_2 emission peak positions monotonically blueshift with increasing film thickness and decreasing compressive in-plane strain ϵ_{xx} . Its plot reveals a strong linear trend (Figure 8c), with slopes equal to 117 meV per % strain ($r^2 = 0.91$)

and 85 meV per % strain ($r^2 = 0.89$) for the A_1 and A_2 emission peaks, respectively.

To ascribe the PL emission peaks observed in this study to specific recombination pathways, we refer to the hybrid functional molecular dynamics simulations of BiVO_4 reported by Wiktor et al.^[54] Their calculated energy diagram, corrected to 300 K for thermal and quantum renormalization effects, shows a bandgap of 2.69 eV, a hole polaron level 0.11 eV above the valence band maximum, and an electron polaron level 0.88 eV below the conduction band minimum. Their calculated bandgap value is very close to our B_1 emission band; we, therefore, attribute this emission to band-to-band recombination. In addition, the ≈ 70 meV separation between the B_1 and B_2 emission peaks agrees in magnitude with the theoretical difference between the hole polaron level and the valence band maximum. The B_2 emission band may thus be ascribed to the recombination between the conduction band electron and hole polaron. Note that the B_1 – B_2 emission

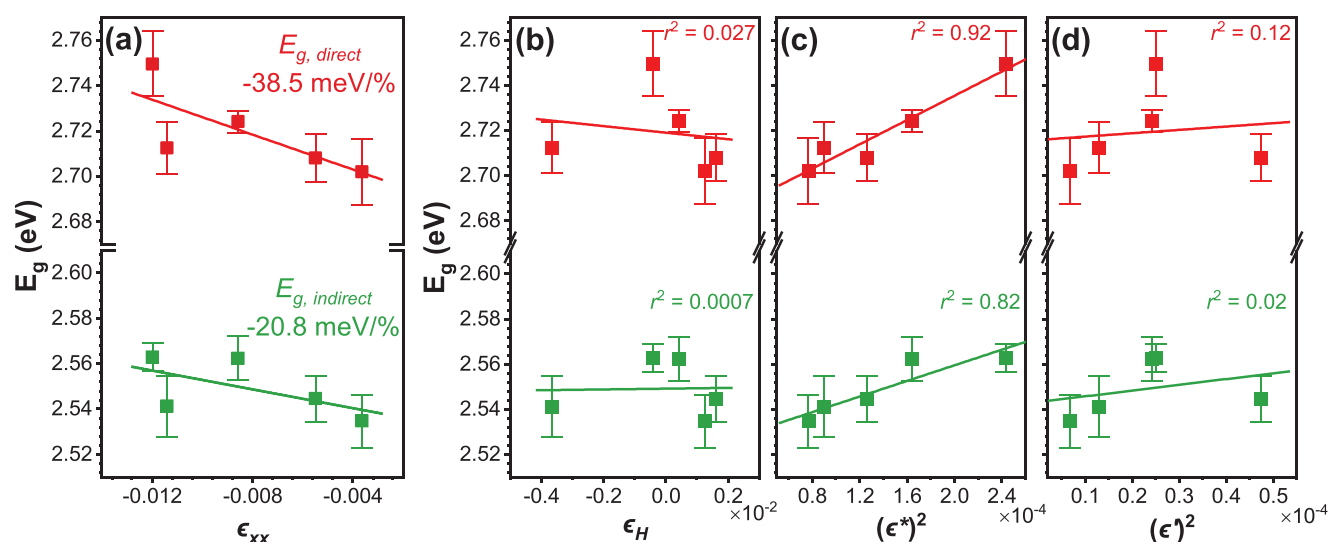


Figure 7. a) Tauc direct and indirect bandgaps of epitaxial BiVO_4 thin films as a function of the in-plane strain along [100], ϵ_{xx} . b–d) Tauc direct and indirect bandgaps plotted with respect to the magnitude of the hydrostatic ϵ_H , and deviatoric strain components $(\epsilon^*)^2$ and $(\epsilon')^2$. The bandgaps strongly correlate with $(\epsilon^*)^2$ but not with ϵ_H and $(\epsilon')^2$. Error bars correspond to 95% confidence intervals from Tauc analysis.

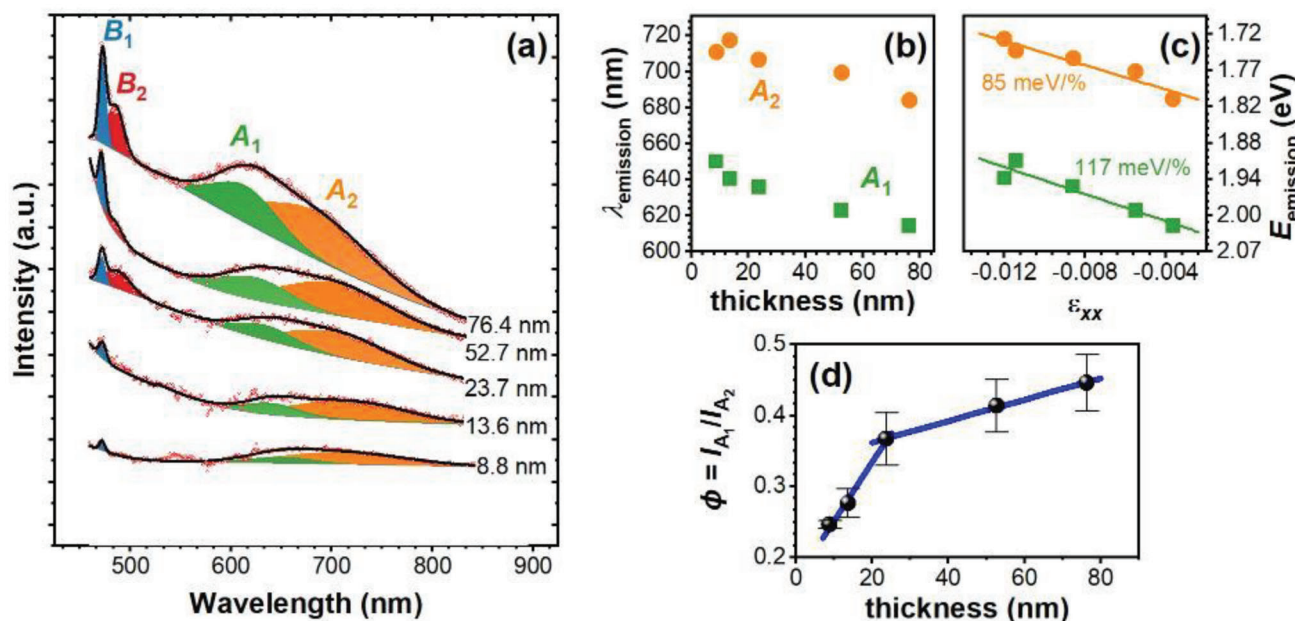


Figure 8. a) Photoluminescence emission spectra of the epitaxial BiVO_4 thin films; A_1 and A_2 photoluminescence emission peak positions as a function of b) film thickness and c) in-plane strain ϵ_{xx} . d) Relative proportions of A_1 and A_2 emission centers in the film N_{A_1}/N_{A_2} as a function of film thickness. Error bars in (d) correspond to standard errors.

peak separation is also close to the thermal hopping activation energy (≈ 90 meV) determined from THz spectroscopy.^[55]

We attribute the broad emission peaks A_1 and A_2 to the radiative recombination of an electron and hole polarons since the observed emission peak positions closely match the calculated energy separation between the electron and hole polaron states (≈ 1.7 eV). This is further supported by the fact that no absorption peaks were found in this region (see Figure 6), indicating that the level(s) responsible for this emission band is not populated in the dark. Similar polaronic photoluminescence signals have also been observed in other oxides like LiNbO_3 and LiTaO_3 .^[56] While the existence and role of polarons in BiVO_4 are supported by theory^[54,57] and experiment,^[55,58,59] understanding the detailed mechanisms involved in the polaronic photoluminescence in BiVO_4 is beyond the scope of this present paper and deserves its own separate investigation.

The possibility of assigning the A_1 and A_2 PL emission peaks to the related electron polaron-free hole (i.e., valence band hole) recombination channel is less likely, as theoretical calculations show that photogenerated holes energetically prefer to be in the polaronic state than as free holes.^[60] Indeed, transient absorption spectroscopy measurements revealed that free holes populate hole polaron states very quickly (≈ 5 ps)^[61] due to the relative proximity of the hole polaron states to the valence band.^[54,62]

With the peak assignments above, it is still unclear whether the splitting of the broad PL emission into A_1 and A_2 peaks is associated with changes in the energy levels of the electron polarons, hole polarons, or both. The electron and hole polaron energetics are connected to the distortions that the VO_4 tetrahedra and BiO_8 dodecahedra^[60] would experience upon imposing anisotropic in-plane strain; discriminating the possible distortion states is therefore essential in order to understand the features observed in the PL emission spectra, even at a qualitative level.

On the basis of our data and available theoretical calculations, we propose that the A_1 and A_2 emission peaks possibly emanate from two distinct populations of BiO_8 dodecahedra in the BiVO_4 films modulated by the anisotropic in-plane strain. This assignment is reasonable since photoluminescence signals of Bi^{3+} have been reported to be sensitive to the local environment.^[63] Moreover, it has been reported that stoichiometric bismuth compounds with off-centered Bi^{3+} positions exhibit broad PL emission peaks,^[64] similar to the broad A_1 and A_2 PL emission peaks observed in this study. Finally, among the structural polyhedral units in BiVO_4 , the BiO_8 dodecahedra are shown to be more susceptible to distortions than the more rigid VO_4 tetrahedra.^[65] The ease at which the BiO_8 dodecahedra gets distorted compared to VO_4 tetrahedra implies that the changes in the electronic structure in BiVO_4 would be largely impacted by distortional changes in the BiO_8 dodecahedra, and less from the VO_4 tetrahedra.

As hole polarons are connected to the localization of photogenerated holes in the BiO_8 dodecahedra,^[60] we then attempt to clarify the nature of the A_1 and A_2 PL emission peaks by relating hole polaron energetics in BiVO_4 to the distortions in the BiO_8 dodecahedra. This relationship may be inferred from the first principle calculations study of Kweon and Hwang,^[60] in which the theoretical energy levels of hole polarons relative to the valence band for nonpolaronic (delocalized) and polaronic (localized) configurations are reported for both monoclinic and tetragonal scheelite BiVO_4 . The calculations indicate that holes in the polaronic configuration, whether in the tetragonal or monoclinic polymorph, tend to localize more around the BiO_8 unit and distort the dodecahedra in the process with a concomitant contraction of some of the Bi–O bonds. Nonpolaronic configurations result in relatively undistorted BiO_8 geometries similar to the ground state BiO_8 geometries. Consequently, holes that form in the polaronic configuration have energy levels located 100 meV deeper into the

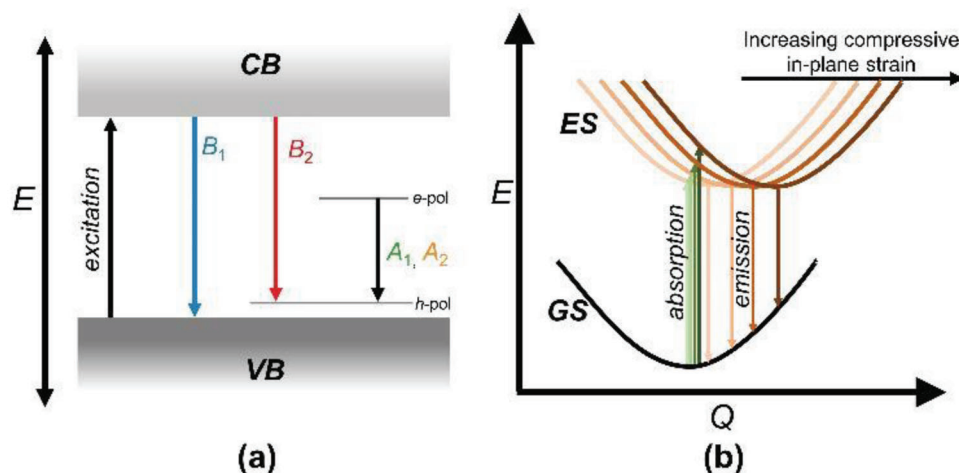


Figure 9. a) Band diagram depicting the radiative recombination transitions observed in photoluminescence spectroscopy after illumination by 405 nm photons. B_1 corresponds to band-to-band recombination, B_2 to conduction band (CB) electron-to-hole polaron (h -pol) recombination, and A_1 , A_2 to electron polaron (e -pol)-hole polaron (h -pol) recombination channels. b) Configurational coordinate (cc) diagram depicting the effect of increasing compressive in-plane strain in the absorption and photoluminescence emission in epitaxial BiVO_4 thin films. Increasing compressive in-plane strain induces a shift of the excited state (ES) potential energy surface to the right of the ground state (GS) minimum due to increased lattice distortion arising from the imposed in-plane strain.

bandgap than the nonpolaronic counterpart. These reported theoretical findings can be extrapolated to generate the following relationship: the more distorted the BiO_8 dodecahedra, the deeper into the bandgap the hole polaron energy level is located; on the other hand, the less distorted the BiO_8 dodecahedra, the closer the hole polaron energy level is to the valence band. We expect that the above picture would hold for BiO_8 distorting processes occurring under volume-preserving lattice deformations, which is the case in our epitaxial BiVO_4 films. Given the above premises, the higher energy A_1 PL emission peak around ≈ 1.95 eV may be assigned to the radiative recombination of an electron polaron with a hole polaron in less distorted BiO_8 populations. The lower energy A_2 PL emission peak around ≈ 1.75 eV may then be assigned to the radiative recombination of an electron polaron with a hole polaron in more distorted BiO_8 populations. The above assignments are depicted in **Figure 9a**. We also designate the less distorted and more distorted BiO_8 populations as A_1 and A_2 PL emission centers, respectively.

Assuming the above assignments for the A_1 and A_2 PL emission centers hold, one would expect the relative PL intensities I_{A_1}/I_{A_2} to change with the degree of BiO_8 distortion. To establish a link between the degree of BiO_8 distortion with film thickness, we refer to another study by Kweon and Hwang,^[66] in which they explored the BiO_8 distortion at the interface in both ts - and ms - BiVO_4 via first-principles calculations. Their results indicate that BiO_8 distortion is more pronounced at the interface than in the bulk for both polymorphs. Although their calculations are performed relative to a vacuum interface, these results may be qualitatively extended to a metal oxide interface. In our films, the BiO_8 units at the BiVO_4/YSZ interface would therefore be more distorted than those further away from the interface. Assuming this to be the case, we infer that the thinner BiVO_4 films that experience larger in-plane strain would have a higher relative proportion of distorted BiO_8 units (that is, more A_2 populations than A_1) than for the thicker films relieved partially of in-plane strain.

If true, this means that the relative integrated PL areas I_{A_1}/I_{A_2} must increase with film thickness.

We clearly see this is indeed the case. **Figure 8d** presents the monotonic increase in the values of the ratio of the integrated PL areas of the A_1 and A_2 emission peaks, $\phi = I_{A_1}/I_{A_2}$, with film thickness. The integrated PL area ratio ϕ , in turn, is related to the relative proportions of the number of A_1 and A_2 emission centers in the film, N_{A_1}/N_{A_2} , since PL emission intensity varies linearly with the population of emission centers. Upon closer inspection, the data may be fitted with two linear trendlines, one steeper than the other, that intersect at around the critical thickness of relaxation $h_c \approx 22$ nm. This suggests that the population of A_2 emission centers appears to be the more dominant emission center relative to the A_1 emission centers for thinner samples. As the film becomes thicker, the population of A_1 emission centers becomes more dominant relative to the A_2 emission centers. The two linear fits seem to suggest two different PL emission regimes across the critical thickness of relaxation h_c . The slope of these fits may be taken to represent the rate at which the population distribution of emission centers changes with thickness. The steeper slope below h_c implies that the population of A_1 emission centers increases rapidly with thickness. Above h_c , the gentler slope implies that the increase in the population of A_1 emission centers is much slower relative to A_2 . The fact that there exist two linear regimes in **Figure 8d** with a transition around h_c further supports that our assignments – that the A_2 emission centers originate from more distorted BiO_8 populations, and A_1 emission centers from less distorted BiO_8 populations – are likely true.

The discussion on the nature of the polaronic photoluminescence in epitaxial BiVO_4 thin films above thus suggests increased hole polaron localization with increasing strain-induced BiO_8 distortion. Since increased hole polaron localization is known to correlate to a decrease in mobility, highly strained BiVO_4 thin films that exhibit a greater degree of BiO_8 distortion may result

in lower photocurrents as compared to the less strained counterparts. Such insight would be the subject of a future study into the epitaxial strain-modulated photoelectrochemical properties of BiVO₄ photoabsorbers.

Finally, we note that the observed trends in the bandgap and A₁ and A₂ photoluminescence emission peak positions with increasing compressive in-plane strain ϵ_{xx} (see Figures 7a and 8c, respectively) are also consistent with the explanations above. This can be qualitatively understood using the configurational coordinate (cc) diagram in Figure 9b. The configuration coordinate Q quantifies the lattice distortion accompanying polaron formation and is related to the square of atomic displacements between ground and excited state geometries.^[67] Following photogeneration of conduction band electrons and valence band holes, carriers localize and form an electron polaron-hole polaron excited state ($e_{pol} + h_{pol}$), with its potential energy surface shifted to the right of the ground state minimum ($Q = 0$) due to the lattice distortion around the polaron. Considering the inferences derived previously, imposing an increasing compressive in-plane strain ϵ_{xx} leads to further distortion of the BiO₈ dodecahedra, which shifts the potential energy surface of the ($e_{pol} + h_{pol}$) excited state further to the right of the ground state. Given the proposed cc diagram, one sees that the energy ΔE required for optical excitations from the ground state to the ($e_{pol} + h_{pol}$) excited state increases with increasing compressive in-plane strain ϵ_{xx} , consistent with the observed widening of the bandgap. At the same time, the transitions from the ($e_{pol} + h_{pol}$) excited state to the ground state decreases with increasing compressive in-plane strain ϵ_{xx} , which agrees well with the redshift in the photoluminescence emission with increasing compressive in-plane strain.

5. Summary

In summary, we demonstrated alternating-target layer-by-layer pulsed laser deposition as an effective method to grow stoichiometric epitaxial BiVO₄ thin films, while avoiding the complexity of optimizing target composition that is necessary for the traditional single-target PLD approach. Using this approach, we were able to grow phase pure monoclinic BiVO₄ films of high structural and crystalline quality, as assessed by a suite of X-ray-based characterization methods, on YSZ substrates. Thickness-dependent studies revealed the presence of effective anisotropic uniaxial in-plane strain in our epitaxial films, which impacts the optical properties and effectively the electronic structure of BiVO₄. Increasing compressive in-plane strain along the [100] direction widens the Tauc-direct and indirect bandgaps of BiVO₄. At the same time, sub-bandgap photoluminescence emission peaks at ≈ 1.75 and ≈ 1.95 eV—attributed to radiative recombination of localized electron and hole polarons—are observed and redshifted with increasing compressive in-plane strain along the [100] direction. Through strain tensor analysis, we found that deviatoric strain, associated with the volume-preserving lattice distortion, is the most important component that influences the optoelectronic properties of epitaxial BiVO₄, while hydrostatic strain does not show any correlation. The deviatoric strain is proposed to introduce distortion to the BiO₈ dodecahedra, which in turn explains the changes observed in the electronic structure of BiVO₄ under the compressive in-plane strain along the [100] direction. Finally, it is important to note that although our

study offers to construct a connection between the distortions of the BiO₈ units in BiVO₄ and hole polaron energetics as a function of the imposed compressive in-plane strain, providing unequivocal geometric experimental data for epitaxial thin films would require Rietveld refinement-like methods to determine the atomic positions for these samples similar to the ones routinely performed in powder X-ray diffraction methods. Local structure-sensitive methods, such as near-edge X-ray absorption fine structure spectroscopy,^[68] to probe the local BiO₈ dodecahedral environment may provide further insights into the local distortional changes to the BiO₈ dodecahedra with imposed compressive in-plane strain. Hard X-ray photoelectron spectroscopy that investigates the BiVO₄/YSZ interface may also be beneficial to further correlate the changes in electronic and chemical properties of this interface with epitaxial strain. Such insights can guide future efforts to improve the efficiency of photoabsorbers through strain engineering.

Supporting Information

Supporting Information is available from the Wiley Online Library or from the author.

Acknowledgements

The authors thank Karsten Harbauer and Dr. Patrick Schnell (PLD), René Schwidessen (HZB X-ray CoreLab Facilities), Dr. Klaus Schwarzburg (photoluminescence spectroscopy), and Dr. Leo Choubrac (Raman spectroscopy) for experimental assistance for this study. The authors also acknowledge the financial support from the Helmholtz International Research School “Hybrid Integrated Systems for Conversion of Solar Energy” (HI-SCORE, Grant Nr. HIRS-0008), an initiative co-funded by the Initiative and Networking Fund of the Helmholtz Association.

Open access funding enabled and organized by Projekt DEAL.

Conflict of Interest

The authors declare no conflict of interest.

Data Availability Statement

The data that support the findings of this study are available from the corresponding author upon reasonable request.

Keywords

epitaxial films, epitaxial strain, pulsed laser deposition

Received: April 10, 2023
Revised: December 12, 2012
Published online:

- [1] J. H. Kim, D. Hansora, P. Sharma, J.-W. Jang, J. S. Lee, *Chem. Soc. Rev.* **2019**, *48*, 1908.
- [2] I. D. Sharp, J. K. Cooper, F. M. Toma, R. Buonsanti, *ACS Energy Lett.* **2017**, *2*, 139.

- [3] I. Y. Ahmet, Y. Ma, J.-W. Jang, T. Henschel, B. Stannowski, T. Lopes, A. Vilanova, A. Mendes, F. F. Abdi, R. van de Krol, *Sustainable Energy Fuels* **2019**, *3*, 2366.
- [4] K. R. Tolod, S. Hernández, N. Russo, *Catalysts* **2017**, *7*, 13.
- [5] Y. Pihosh, I. Turkevych, K. Mawatari, J. Uemura, Y. Kazoe, S. Kosar, K. Makita, T. Sugaya, T. Matsui, D. Fujita, *Sci. Rep.* **2015**, *5*, 11141.
- [6] H. Cai, W. Zhao, G. Xiao, Y. Hu, X. Wu, H. Ni, S. Ikeda, Y. Ng, J. Tao, L. Zhao, F. Jiang, *Adv. Sci.* **2023**, *10*, 2205726.
- [7] Y. Qiu, W. Liu, W. Chen, W. Chen, G. Zhou, P. C. Hsu, R. Zhang, Z. Liang, S. Fan, Y. Zhang, Y. Cui, *Sci. Adv.* **2016**, *2*, 1501764.
- [8] F. F. Abdi, A. Dabirian, B. Dam, R. van de Krol, *Phys. Chem. Chem. Phys.* **2014**, *16*, 15272.
- [9] J. Kouvetakis, J. Menendez, A. V. G. Chizmeshya, *Annu. Rev. Mater. Res.* **2006**, *36*, 497.
- [10] H. Ye, J. Yu, *Sci. Technol. Adv. Mater.* **2014**, *15*, 024601.
- [11] L. Balaghi, G. Bussone, R. Grifone, R. Hubner, J. Grenzer, M. Ghorbani-Asl, A. V. Krasheninnikov, H. Schneider, M. Helm, E. Dimakis, *Nat. Commun.* **2019**, *10*, 2793.
- [12] N. Vonrüti, U. Aschauer, *Phys. Rev. Mater.* **2018**, *2*, 105401.
- [13] A. Vailionis, in *Epitaxial Growth of Complex Metal Oxides*, 2nd ed. (Eds: G. Koster, M. Huijben, G. Rijnders), Woodhead Publishing, Cambridge, USA **2022**, Ch. 7.
- [14] L. Gu, D. Li, L. Chao, H. Dong, W. Hui, T. Niu, C. Ran, Y. Xia, L. Song, Y. Chen, W. Huang, *Sol. RRL* **2021**, *5*, 2000672.
- [15] Z. Huang, Z. Q. Liu, M. Yang, S. W. Zeng, A. Annadi, W. M. Lü, X. L. Tan, P. F. Chen, L. Sun, X. Renshaw Wang, Y. L. Zhao, C. J. Li, J. Zhou, K. Han, W. B. Wu, Y. P. Feng, J. M. D. Coey, T. Venkatesan, Ariando, *Phys. Rev. B* **2014**, *90*, 125156. [CrossRef]
- [16] M. Chu, Y. Sun, U. Aghoram, S. E. Thompson, *Annu. Rev. Mater. Res.* **2009**, *39*, 203.
- [17] J. Jiang, X. Sun, X. Chen, B. Wang, Z. Chen, Y. Hu, Y. Guo, L. Zhang, Y. Ma, L. Gao, F. Zheng, L. Jin, M. Chen, Z. Ma, Y. Zhou, N. P. Padture, K. Beach, H. Terrones, Y. Shi, D. Gall, T. M. Lu, E. Wertz, J. Feng, J. Shi, *Nat. Commun.* **2019**, *10*, 4145.
- [18] R. Karim, C. Vittoria, *J. Magn. Magn. Mater.* **1997**, *167*, 27.
- [19] A. J. E. Rettie, S. Mozaffari, M. D. McDaniel, K. N. Pearson, J. G. Ekerdt, J. T. Markert, C. B. Mullins, *J. Phys. Chem. C* **2014**, *118*, 26543.
- [20] P. R. Willmott, J. R. Huber, *Rev. Mod. Phys.* **2000**, *72*, 315.
- [21] T. Ohnishi, K. Shibuya, T. Yamamoto, M. Lippmaa, *J. Appl. Phys.* **2008**, *103*, 103703.
- [22] M. Strikovski, J. H. Miller, *Appl. Phys. Lett.* **1998**, *73*, 1733.
- [23] Q. Lei, M. Golalikhani, B. A. Davidson, G. Liu, D. G. Schlom, Q. Qiao, Y. Zhu, R. U. Chandrasena, W. Yang, A. X. Gray, E. Arenholz, A. K. Farrar, D. A. Tenne, M. Hu, J. Guo, R. K. Singh, X. Xi, *npj Quantum Mater.* **2017**, *2*, 10.
- [24] M. Bjorck, G. Andersson, *J. Appl. Crystallogr.* **2007**, *40*, 1174.
- [25] P. Manley, G. Yin, M. Schmid, *J. Phys. D: Appl. Phys.* **2014**, *47*, 205301.
- [26] A. B. Kuzmenko, *Rev. Sci. Instrum.* **2005**, *76*, 083108.
- [27] J. A. Krogstad, M. Lepple, Y. Gao, D. M. Lipkin, C. G. Levi, *J. Am. Ceram. Soc.* **2011**, *94*, 4548.
- [28] A. W. Sleight, H. y. Chen, A. Ferretti, D. E. Cox, *Mater. Res. Bull.* **1979**, *14*, 1571.
- [29] H. N. Lee, S. Senz, N. D. Zakharov, C. Harnagea, A. Pignolet, D. Hesse, U. Gösele, *Appl. Phys. Lett.* **2000**, *77*, 3260.
- [30] S. Jun, Y. S. Kim, J. Lee, Y. W. Kim, *Appl. Phys. Lett.* **2001**, *78*, 2542.
- [31] Q. X. Jia, S. G. Song, X. D. Wu, J. H. Cho, S. R. Foltyn, A. T. Findikoglu, J. L. Smith, *Appl. Phys. Lett.* **1996**, *68*, 1069.
- [32] D. Dubbink, G. Koster, G. Rijnders, *Sci. Rep.* **2018**, *8*, 5774.
- [33] J. Song, M. J. Seo, T. H. Lee, Y.-R. Jo, J. Lee, T. L. Kim, S.-Y. Kim, S.-M. Kim, S. Y. Jeong, H. An, S. Kim, B. H. Lee, D. Lee, H. W. Jang, B.-J. Kim, S. Lee, *ACS Catal.* **2018**, *8*, 5952.
- [34] M. Kamei, T. Yagami, S. Takaki, Y. Shigesato, *Appl. Phys. Lett.* **1994**, *64*, 2712.
- [35] S. Ke, C. Chen, N. Fu, H. Zhou, M. Ye, P. Lin, W. Yuan, X. Zeng, L. Chen, H. Huang, *ACS Appl. Mater. Interfaces* **2016**, *8*, 28406.
- [36] P.-C. Wu, Y.-P. Lin, Y.-H. Juan, Y.-M. Wang, D. Thi-Hien, H.-Y. Chang, Y.-H. Chu, *ACS Appl. Nano Mater.* **2018**, *1*, 6890.
- [37] S. Wang, S. Feng, B. Liu, Z. Gong, T. Wang, J. Gong, *Chem. Sci.* **2023**, *14*, 2192.
- [38] S. Stoughton, M. Showak, Q. Mao, P. Koirala, D. A. Hillsberry, S. Sallis, L. F. Kourkoutis, K. Nguyen, L. F. J. Piper, D. A. Tenne, N. J. Podraza, D. A. Muller, C. Adamo, D. G. Schlom, *APL Mater.* **2013**, *1*, 042112.
- [39] Y. Liang, T. Tsubota, L. P. A. Mooij, R. van de Krol, *J. Phys. Chem. C* **2011**, *115*, 17594.
- [40] V. Kaganer, M. Schmidbauer, R. Opitz, B. Jenichen, R. Köhler, *Phys. Rev. B* **1996**, *55*, 1793.
- [41] R. W. Ulbricht, A. Schmehl, T. Heeg, J. Schubert, D. G. Schlom, *Appl. Phys. Lett.* **2008**, *93*, 102105.
- [42] P. Müller, P. Turban, L. Lapena, S. Andrieu, *Surf. Sci.* **2001**, *488*, 52.
- [43] a) D. Schick, A. Bojahr, M. Herzog, P. Gaal, I. Vrejoiu, M. Bargheer, *Phys. Rev. Lett.* **2013**, *110*, 095502; b) C. J. M. Daumont, S. Farokhipoor, A. Ferri, J. C. Wojdeł, J. Iñiguez, B. J. Kooi, B. Noheda, *Phys. Rev. B* **2010**, *81*, 144115; c) A. Fernandez, L. Caretta, S. Das, C. Klewe, D. Lou, E. Parsonnet, R. Gao, A. Luo, P. Shafer, L. W. Martin, *Adv. Energy Mater.* **2021**, *11*, 2102175; d) D. Colombara, F. Werner, T. Schwarz, I. Canero Infante, Y. Fleming, N. Valle, C. Spindler, E. Vacchieri, G. Rey, M. Guennou, M. Bouttemy, A. G. Manjon, I. Peral Alonso, M. Melchiorre, B. El Adib, B. Gault, D. Raabe, P. J. Dale, S. Siebentritt, *Nat. Commun.* **2018**, *9*, 826.
- [44] J. Bardeen, W. Shockley, *Phys. Rev.* **1950**, *80*, 72.
- [45] W. I. F. David, I. G. Wood, *J. Phys. C: Solid State Phys.* **1983**, *16*, 5127.
- [46] S.-H. Wei, A. Zunger, *Phys. Rev. B* **1999**, *60*, 5404.
- [47] D. Errandonea, A. B. Garg, *Prog. Mater. Sci.* **2018**, *97*, 123.
- [48] A. Kuzmin, A. Anspoks, A. Kalinko, J. Timoshenko, R. Kalendarev, *Sol. Energy Mater. Sol. Cells* **2015**, *143*, 627.
- [49] P. Yu, M. Cardona, *Fundamentals of Semiconductors: Physics and Materials Properties*, Springer, Berlin **2007**.
- [50] P. F. Newhouse, D. Guevarra, M. Umehara, S. E. Reyes-Lillo, L. Zhou, D. A. Boyd, S. K. Suram, J. K. Cooper, J. A. Haber, J. B. Neaton, J. M. Gregoire, *Energy Environ. Sci.* **2018**, *11*, 2444.
- [51] T. Tachikawa, T. Ochi, Y. Kobori, *ACS Catal.* **2016**, *6*, 2250.
- [52] Y. Sasaki, H. Nemoto, K. Saito, A. Kudo, *J. Phys. Chem. C* **2009**, *113*, 17536.
- [53] J. K. Cooper, S. B. Scott, Y. Ling, J. Yang, S. Hao, Y. Li, F. M. Toma, M. Stutzmann, K. V. Lakshmi, I. D. Sharp, *Chem. Mater.* **2016**, *28*, 5761.
- [54] J. Wiktór, F. Ambrosio, A. Pasquarello, *ACS Energy Lett.* **2018**, *3*, 1693.
- [55] M. Ziwrtsch, S. Müller, H. Hempel, T. Unold, F. F. Abdi, R. van de Krol, D. Friedrich, R. Eichberger, *ACS Energy Lett.* **2016**, *1*, 888.
- [56] P. Reichenbach, T. Kämpfe, A. Haufmann, A. Thiessen, T. Woike, R. Steudtner, L. Kocsor, Z. Szaller, L. Kovács, L. M. Eng, *Crystals* **2018**, *8*, 214.
- [57] K. E. Kweon, G. S. Hwang, J. Kim, S. Kim, S. Kim, *Phys. Chem. Chem. Phys.* **2015**, *17*, 256.
- [58] V. Jovic, J. Laverock, A. J. E. Rettie, J. S. Zhou, C. B. Mullins, V. R. Singh, B. Lamoureux, D. Wilson, T. Y. Su, B. Jovic, H. Bluhm, T. Söhnel, K. E. Smith, *J. Mater. Chem. A* **2015**, *3*, 23743.
- [59] M. Mohamed, M. M. May, M. Kanis, M. Brützmam, R. Uecker, R. van de Krol, C. Janowitz, M. Mulazzi, *RSC Adv.* **2019**, *9*, 15606.
- [60] K. E. Kweon, G. S. Hwang, *Phys. Rev. B* **2013**, *87*, 205202.
- [61] J. Ravensbergen, F. F. Abdi, J. H. van Santen, R. N. Frese, B. Dam, R. van de Krol, J. T. M. Kennis, *J. Phys. Chem. C* **2014**, *118*, 27793.
- [62] a) J. K. Cooper, S. E. Reyes-Lillo, L. H. Hess, C.-M. Jiang, J. B. Neaton, I. D. Sharp, *J. Phys. Chem. C* **2018**, *122*, 20642; b) Y. Suzuki, D. H. K. Murthy, H. Matsuzaki, A. Furube, Q. Wang, T. Hisatomi, K. Domen, K. Seki, *J. Phys. Chem. C* **2017**, *121*, 19044.

- [63] P. Boutinaud, *Inorg. Chem.* **2013**, *52*, 6028.
- [64] C. W. M. Timmermans, G. Blasse, *J. Solid State Chem.* **1984**, *52*, 222.
- [65] J. W. E. Mariathasan, R. M. Hazen, L. W. Finger, *Phase Transitions* **1986**, *6*, 165.
- [66] K. E. Kweon, G. S. Hwang, *Appl. Phys. Lett.* **2013**, *103*, 131603.
- [67] A. Alkauskas, Q. Yan, C. G. Van de Walle, *Phys. Rev. B* **2014**, *90*, 075202.
- [68] Y. Uemura, D. Kido, A. Koide, Y. Wakisaka, Y. Niwa, S. Nozawa, K. Ichianagi, R. Fukaya, S.-I. Adachi, T. Katayama, T. Togashi, S. Owada, M. Yabashi, K. Hatada, A. Iwase, A. Kudo, S. Takakusagi, T. Yokoyama, K. Asakura, *Chem. Commun.* **2017**, *53*, 7314.